Measuring the Quenching Timescales of Milky Way Satellites with *Gaia* Proper Motions

Sean P. Fillingham,[1]⋆ Michael C. Cooper,[1] Tyler Kelley,[1]
Michael Boylan-Kolchin,[2] James S. Bullock,[1]

[1]*Center for Cosmology, Department of Physics & Astronomy, University of California, Irvine, 4129 Reines Hall, Irvine, CA 92697, USA*
[2]*Department of Astronomy, The University of Texas at Austin, 2515 Speedway, Stop C1400, Austin, TX 78712, USA*

3 October 2018

ABSTRACT

Awesomeness with *Gaia* DR2 proper motions...flogging (beating) the dead horse that is environmental quenching in the Local Group....

Key words: Local Group – galaxies: dwarf – galaxies: evolution – galaxies: star formation – galaxies: formation – galaxies: general

1 INTRODUCTION

Large surveys of the nearby Universe show that galaxies at (and below) the mass scale of the Magellanic clouds (10^6 M$_\odot \lesssim M_\star \lesssim 10^9$ M$_\odot$) are predominantly star forming in the field (Haines et al. 2008; Geha et al. 2012). This stands in stark contrast to the population of low-mass galaxies that currently reside near a more massive host system, where the fraction of systems that are no longer forming stars (i.e. "quenched") is significantly larger (Geha et al. 2012; Wheeler et al. 2014; Phillips et al. 2015). For dwarfs with $M_\star \lesssim 10^8$ M$_\odot$ in the Local Volume, this field-satellite dichotomy is very apparent, with satellites of the Milky Way (MW) and M31 being largely gas-poor, passive systems in contrast to the gas-rich, star-forming field population (e.g. Mateo 1998; Grcevich & Putman 2009; Spekkens et al. 2014). This clear distinction between the field and satellite populations strongly favors environmental processes as the dominant quenching mechanisms in this low-mass regime ($M_\star \lesssim 10^8$ M$_\odot$, Lin & Faber 1983; Slater & Bell 2014; Weisz et al. 2015; Wetzel et al. 2015; Fillingham et al. 2015, 2016, 2018).

At the very lowest mass scales (i.e. the regime of ultra-faint dwarfs), however, there is evidence for a transition in the dominant quenching mechanism from one associated with galaxy environment to one driven by reionization. The universally old stellar populations observed in the ultra-faint dwarfs (UFDs) suggest that star formation on the smallest galactic scales is suppressed at very early times and across all environments, marking a significant transition in the dominant quenching mechanism at the lowest masses (Brown et al. 2014; Rodriguez Wimberly et al. 2018).

Across all mass scales, some of the most powerful studies of satellite quenching have utilized measurements of satellite and field quenched fractions to infer the timescale upon which satellite quenching occurs following infall (e.g. Wetzel et al. 2013; Fillingham et al. 2015; Balogh et al. 2016). These studies point to a picture where quenching proceeds relatively slowly at high masses, consistent with quenching via starvation (Fillingham et al. 2015). Below some host-dependent critical mass scale, however, quenching is rapid, as stripping becomes increasingly efficient (Fillingham et al. 2016). In defining this model of satellite quenching, simulations are commonly utilized to constrain the distribution of infall times for an observed sample of satellites. This statistical approach is required, as it is extremely difficult to infer the infall time for a significant fraction of the satellite population in even the most nearby groups and clusters. Moreover, in systems more distant than ∼ 1 Mpc, it is difficult to measure a precise star-formation history via spatially-resolved stellar photometry, even with the aid of imaging from the *Hubble Space Telescope* (*HST*). Within the LG, however, we are afforded the luxury of more detailed observations of the nearby satellite and field populations. This is particularly true with the release of *Gaia* Data Release 2 (DR2, Gaia Collaboration et al. 2016a, 2018a), which now enables an investigation of satellite quenching timescales (measured relative to infall) on an object-by-object basis. This offers a unique opportunity to test the results of large statistical analyses and our current physical picture of satellite quenching.

In this work, we aim to determine the quenching timescale and ultimately constrain the potential mechanisms responsible for suppressing star formation in individual MW satellite galaxies. Utilizing the latest data products from *Gaia* DR2 (Gaia Collaboration et al. 2018a,b), we infer the cosmic time when each dwarf galaxy around the MW became a satellite (i.e. the infall time) through comparison to cosmological *N*-body simulations. In addition, we infer the quenching times for the MW satellites based on their published star-formation histories, as derived from *HST* imaging (Weisz et al. 2014, 2015; Brown et al. 2014). Finally, through comparison of the quenching times to the infall times, we will characterize the quenching timescales for each object and constrain the potential

⋆ e-mail: sfilling@uci.edu

mechanisms responsible for quenching each MW satellite galaxy. In §2, we discuss our sample of local dwarfs and the methodology by which we measure the infall and quenching time for each system. Our primary results are presented in §3, followed by a discussion of how these results connect to physical models of satellite quenching in §4. Finally, we summarize our results and conclusions in §5. Where necessary, we adopt a ΛCDM cosmology with the following parameters: $\sigma_8 = 0.815$, $\Omega_m = 0.3121$, $\Omega_\Lambda = 0.6879$, $n_s = 0.9653$, and $h = 0.6751$ (Planck Collaboration et al. 2016), consistent with the simulations used in this work.

2 MILKY WAY DWARF GALAXIES

As shown in Table 1, our sample of local dwarfs is selected from Fritz et al. (2018), including *XXX* systems for which the Gaia DR2 dataset yields a proper motion measurement. Combined with measurements of line-of-sight velocity and distance from the literature, the *Gaia* observations constrain the Galactocentric position and 3D velocity of each system (i.e. full 6D phase-space information). For those galaxies located within a Galactocentric distance of 300 kpc (i.e. within what we assume to be the virial radius of the Milky Way), *HST*/WFCP2 and ACS imaging of 15 yields estimates of their star-formation history. These 15 dwarfs comprise our primary sample and span a stellar mass range of $M_\star \sim 10^{3.5-8}$ M$_\odot$. All of the systems show no evidence of ongoing star formation, with minimal H I reservoirs ($M_{\rm HI} < 0.1\,M_\star$, Grcevich & Putman 2009; Spekkens et al. 2014). While this sample is undoubtedly incomplete below $M_\star \sim 10^{5.5}$ M$_\odot$ (Irwin 1994; Tollerud et al. 2008), our analysis focuses on the potential quenching mechanism for each system individually, such that it does not rely strongly on uniformly sampling the MW satellite population. The largest source of incompleteness is expected to be the limited sky coverage of imaging surveys such as the Sloan Digital Sky Survey (York et al. 2000) and the Dark Energy Survey (Dark Energy Survey Collaboration et al. 2016), which should not be significantly correlated with the accretion history of the satellite population.

To better constrain the physical mechanisms responsible for quenching the low-mass satellites of the Milky Way, we aim to characterize the quenching timescale for each system. As we define more explicitly below, the quenching timescale is the difference between the infall time and the quenching time — i.e. the time that a satellite spends, following infall, prior to having its star formation suppressed. To infer the quenching timescale, we must first measure the quenching time and infall time for each galaxy in our sample.

2.1 Quenching Time

A galaxy's star-formation history (SFH) provides a direct constraint on the epoch at which a galaxy quenched. For nearby galaxies, where the stellar population can be resolved and imaging can reach the oldest main sequence turn-off population, we can constrain the SFH with relative precision (Dolphin 1997; Weisz et al. 2011). Here, we adopt the lookback time at which a galaxy forms 90% of its present day stellar mass (t_{90}) to be the quenching time. Following Weisz et al. (2015), we utilize t_{90} (versus t_{100}) to minimize the potential uncertainty associated with the modeling of blue straggler populations. *Our results are qualitatively unchanged when adopting t_{95} or t_{100}? What is the median difference between t_{90} and t_{95} for our sample?*

For 15 of the dwarfs in our sample (see Table 1), there are published star-formation histories from Weisz et al. (2014) and

Brown et al. (2014), based on *HST*/WFPC2 and ACS imaging. In the case of three systems (all UFDs), the SFH is measured by both Brown et al. (2014) and Weisz et al. (2014), with excellent agreement between the two datasets for Hercules and Leo IV. For the third dwarf in common (CVn II), Weisz et al. (2014) find a more extended SFH, in contrast to the largely ancient stellar population inferred by Brown et al. (2014). Given that the *HST*/WPFC2 imaging analyzed by Weisz et al. (2014) is shallower and covers a smaller area than the *HST*/ACS imaging employed by Brown et al. (2014), we opt to utilize the SFH from Brown et al. (2014). Even allowing for the more extended SFH measured by Weisz et al. (2014), our results are qualitatively unchanged, such that we find CVn II quenches prior to infall.

To determine the time at which each system formed 90% of its stellar mass (t_{90}), we linearly interpolate the measured SFHs from Weisz et al. (2014), using the published data tables (Weisz et al. 2017). As shwon in Figure 2 for Leo II, the corresponding uncertainty in t_{90} is determine by similarly interpolating and evaluating the SFHs including their associated 1σ random and systematic errors. For the remaining 6 systems in our sample, we visually inspect each published SFH from Brown et al. (2014) to measure t_{90}. In particular, utilizing the 1σ confidence intervals from Figure 8 of Brown et al. (2014), we select the lookback time at which the upper and lower bounds of the SFH reach 90% of the present day mass of the system. The average of these two times is taken to be t_{90}. For Hercules and Leo IV, we find a very minor difference between the t_{90} inferred from using the Weisz et al. (2014) dataset and from visually inspecting the Brown et al. (2014) results ($\pm 0.XX$ Gyr). The t_{90} measurements for each system in our sample, which we take to be the quenching time $t_{\rm quench}$, are listed in Table 1 along with their corresponding uncertainties.

2.2 Infall Time

For low-mass dwarfs in the Local Volume, there is a stark difference in the star-forming properties of those within the virial radius ($\sim$ 300 kpc) of either the MW or M31 and those in the field (e.g. Spekkens et al. 2014). While it is uncertain as to the exact physical scale at which environmental effects begin to affect satellite galaxies, this observed field-satellite dichotomy makes a strong case that infall onto the host system (as defined by crossing within the host's virial radius) marks the onset of environmental quenching. In order to constrain the quenching timescale, we must infer the infall time – i.e. the time at which a satellite crosses within the virial radius of the host – for each dwarf in our primary sample.

2.2.1 Gaia *Proper Motions*

The *Gaia* mission recently transformed the observational landscape, providing proper motion measurements for stars in a large number of local dwarfs (Gaia Collaboration et al. 2016a,b, 2018a). Using these data, several studies inferred proper motions for the Milky Way satellites, utilizing various membership criteria (Gaia Collaboration et al. 2018b; Simon 2018; Fritz et al. 2018; Pace & Li 2018; Kallivayalil et al. 2018; Massari & Helmi 2018). *Here, we use the data from Fritz, as it provides the most comprehensive set of proper motion measures for the MW satellite population...Fritz's values agree well with that from the other studies (discuss outliers, if any; talk to Katy). All of these various works are consistent with each other to within the reported errors.*

From Fritz et al. (2018), we adopt the Galactocentric distance,

Galaxy Name	$\log_{10}(M_\star/M_\odot)$ (1)	D_{host} (kpc) (2)	V_{total} (km s^{-1}) (3)	t_{infall} (Gyr) (4)	t_{quench} (Gyr) (5)
Sagittarius	7.322	19.0	316.31	10.55	3.40
Fornax	7.301	149.0	159.71	8.55	2.24
Leo I	6.740	257.0	183.48	2.12	1.68
Sculptor	6.362	86.0	197.16	7.33	10.59
Leo II	5.869	236.0	118.81	7.58	6.41
Carina	5.748	107.0	166.44	9.84	3.00
Draco I	5.452	76.0	160.50	10.24	10.14
Ursa Minor	5.452	78.0	154.43	10.24	11.30
Canes Venatici I	5.372	218.0	142.78	9.25	9.00
Hercules	4.572	126.0	211.67	7.15	11.90
Bootes I	4.456	64.0	194.69	10.26	12.70
Leo IV	4.268	155.0	355.66	10.24	12.20
Ursa Major I	4.144	102.0	261.45	1.53	11.40
Canes Venatici II	3.900	161.0	217.80	1.07	12.60
Coma Bernices I	3.572	45.0	285.72	7.13	13.10

Table 1. *mcc – probably need less precision on some of the values here. also, add errors for infall time and quenching time?* The properties of satellite galaxies of the Milky Way used in this study organized by stellar mass, with the most massive dwarf galaxies at the top. (1) The inferred stellar mass based on the V-band absolute magnitude and assuming $M/L = 1$ (McConnachie 2012). (2) The distance from the center of the MW in kpc (Fritz et al. 2018). (3) The total velocity, in km s^{-1} in the Galactocentric frame-of-reference (Fritz et al. 2018). (4) The infall time, in Gyr, from matching the observed binding energy to the subhalo binding energy distribution in the simulations. (5) The quenching time, in Gyr, inferred from the SFHs by adopting the lookback-time at which the dwarf galaxy formed 90% of its current stellar mass (Weisz et al. 2014; Brown et al. 2014).

radial velocity, and tangential velocity measures for each system in Table 1. Using this phase-space information, we match the MW dwarf galaxies to a respective subhalo populations in cosmological N-body simulations in an effort to constrain their infall times.

2.2.2 Simulations

To determine the infall time of each Milky Way satellite in our sample, we utilize the "ELVIS at the Disco" suite of 12 high-resolution, dissipationless simulations of Milky Way-like halos run with an analytic potential mimicking the effects of a central disk galaxy (Kelley et al. in prep). The suite includes 12 isolated halos simulated within high-resolution uncontaminated volumes spanning $1 - 3$ Mpc in size and using a particle mass of 2.92×10^4 M$_\odot$ and a Plummer equivalent force softening of $\epsilon = 25$ physical parsecs. Within the high-resolution volumes, the halo catalogs are complete down to $M_{\text{halo}} > 3 \times 10^6$ M$_\odot$, $V_{\text{max}} > 4.5$ km s^{-1}, $M_{\text{peak}} > 8 \times 10^6$ M$_\odot$, and $V_{\text{peak}} > 5$ km s^{-1} — therefore more than sufficient to track the evolution and infall time of halos hosting MW dwarfs with $M_\star > 10^{3.5}$ M$_\odot$. The simulations adopt a cosmological model with the following ΛCDM parameters: $\sigma_8 = 0.815$, $\Omega_m = 0.3121$, $\Omega_\Lambda = 0.6879$, $n_s = 0.9653$, and $h = 0.6751$ (Planck Collaboration et al. 2016).

For all subhalos with $M_{\text{peak}} > 10^8$ M$_\odot$, we determine their infall time, defined to be the first timestep when the subhalo passes within the host virial radius. *mcc – what about last infall? does this change the results? make plot of t-infall-first versus t-infall-last for each of the MW sats in sample.* On average, there are XX subhalos per host with the 100% scatter ranging from XX to XX. ***Check the subhalo mass range for each host, essentially what is the most massive subhalo included in the analysis. Is there a mass dependence for either the infall time or binding energy calculation? In other words, should we be including a mass cut in our matching routine, I hope not since that would dramatically reduce our already poor statistics...worth looking into though.*** All

of the subhalos from each simulation box are combined into one final catalog when compared to the MW satellite population.

To facilitate constraining the infall time for each MW dwarf galaxy, we match the observed 6D phase-space properties of the MW satellites to subhalo properties in the simulations. Using the measured infall time for each subhalo, we can map the infall time distributions to the phase-space distributions in the simulations. A useful method for mapping these two distributions was presented in Rocha et al. (2012), where they found a very strong correlation between the present day binding energy of the subhalos in simulations and their infall times. We will use a modified version of the subhalo binding energy presented in Rocha et al. (2012) in order to match the observed binding energies to the subhalo properties, thereby constraining the possible distribution of infall times for each MW satellite.

2.2.3 Binding Energy

As shown by Rocha et al. (2012), the binding energy, $\mathcal{E}$, of a dark matter subhalo strongly correlates with its infall time, such that early accreted subhalos have higher binding energies. Following Rocha et al. (2012), we define the binding energy of a subhalo (or local dwarf) as

$$\mathcal{E} = -\phi(R) - \frac{1}{2}V^2 \,, \tag{1}$$

where $\phi(R)$ is the potential of the subhalo (or MW dwarf galaxy) at the host-centric radial distance, R, and $1/2V^2$ corresponding to the kinetic energy of the subhalo (or galaxy), with V representing the magnitude of the 3D host-centric velocity vector.

mcc – Sean will remake Figure 2 of Rocha et al. (2012) for Tyler's sims.

To determine the potential of each satellite galaxy and subhalo we assume the host mass is distributed in an NFW potential (Navarro et al. 1997), for which we increase the halo concentration to account
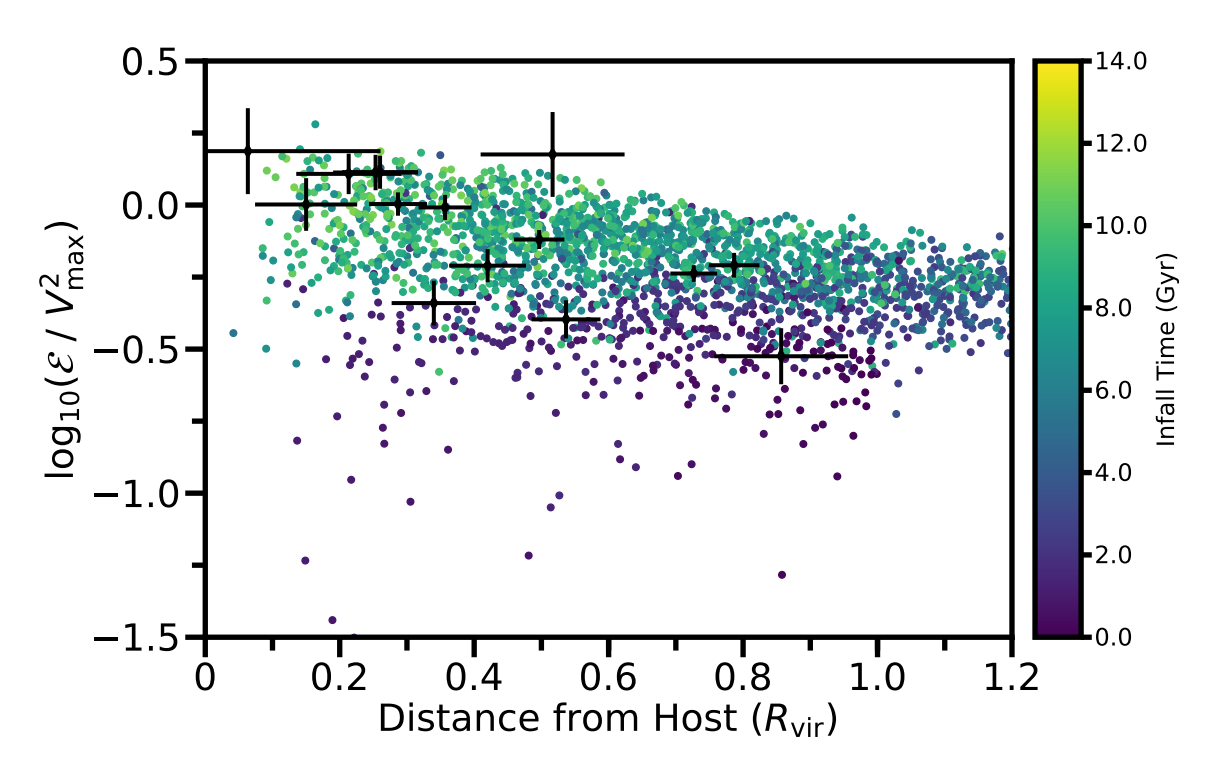
Figure 1. The binding energy ($\mathcal{E}$), scaled by the present day V_{max} of the host, as a function of distance from the host, in units of host R_{vir} for subhalos in the "ELVIS at the Disco" simulation suite. Each point is color-coded by the lookback time to first infall for the subhalo. The black diamonds correspond to the Milky Way dwarfs, assuming $M_{\mathrm{vir}} = 1.3 \times 10^{12}$ M$_\odot$, $R_{\mathrm{vir}} = 300$ kpc, and $R_{\mathrm{s}} = 18.75$ kpc. *To constrain t_{infall}, we select the 15 subhalos closest to each MW dwarf that also have the same directionality in the radial velocity component, in order to determine the distribution of infall times. The error bars illustrate the selection region for each MW dwarf based on the selection criteria, see §2 for more details. As is clearly evident, there exists a strong gradient in infall time as one moves through this parameter space. Many of the Milky Way dwarfs reside in regions with well defined infall times. This allows us to strongly constrain the characteristic infall time for each MW dwarf galaxy.*

for the contribution of the host's baryonic component:

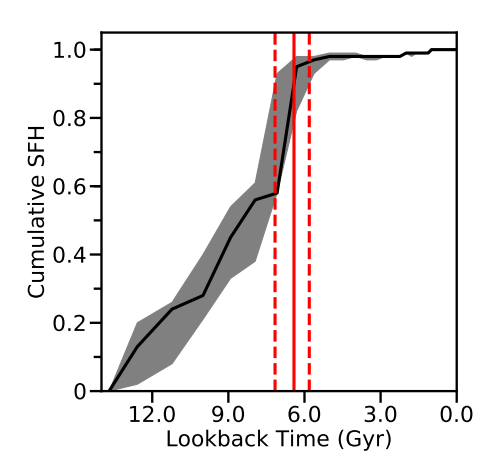$$\phi(r) = -4\pi G \rho_0 r_s^2 \frac{\ln(1 + r/r_s)}{r/r_s}, \qquad (2)$$

where G is the gravitational constant, ρ_0 is the average density of the dark matter halo, and r_s is the scale radius. We define $\phi(R_0) = 0$ with $R_0 = 5$ Mpc. Varying the distance where we anchor the potential does not significantly affect the binding energy measurement or the subsequent distribution of infall times for each MW dwarf galaxy. Adopting $R_0 = 5$ Mpc ensures that the anchor point is well outside the virial radius of the host for all of cosmic time. The simulations include hosts spanning a range of virial masses, and we use the virial radius and scale radius as given in the (soon-to-be-published) halo catalogs to determine the concentration of the host halo. For the suite of 12 hosts, the median concentration is $c \sim 16$.

Due the variation in the host virial masses across the simulation suite, the absolute normalization of the binding energy also varies from host-to-host. Essentially, the subhalos of more massive hosts have larger binding energies on average, due to their deeper potentials. To better compare the simulations to the observational data, we combine the subhalo populations across the various simulation boxes. We "normalize" the binding energy of each satellite by dividing the measured binding energy by the present day maximum circular velocity of the host. For the MW dwarfs, we assume the host potential is an NFW with the following properties: $M_{\mathrm{vir}} = 1.3 \times 10^{12}$ M$_\odot$, $R_{\mathrm{vir}} = 300$ kpc, and $R_{\mathrm{s}} = 18.75$ kpc (Bland-Hawthorn & Gerhard 2016).

2.2.4 Subhalo Matching

It is worth noting that both the binding energy and the radial distance from the host are scalar quantities. Through inclusion of some of the vector information we can further constrain the infall distributions leading to two selection criteria, essentially a vector-based selection followed by the scalar-based selection. First, we select all subhalos with radial velocity components in the same direction as the dwarf galaxy in question (i.e. since Leo I has a positive radial velocity, we first select all of the subhalos that also have positive radial velocities). With the remaining subhalos, we select the 15 nearest to the Milky Way dwarf in the binding energy - radial distance space, see Figure 1. This effectively becomes a density selection in the binding energy - distance space, as the MW satellites that reside in lower density regions will sample a larger region and vice versa, see the error bars in Figure 1. ***Is this the best selection choice? Is there a significant difference is we change how we match MW sats to subhalos?***

We smooth the selected infall time distribution with a gaussian kernel of width 0.8 in an effort to better characterize the underlying distribution free of noise smaller than the kernel size, see Figure 2. Varying the kernel width does not have a significant impact on the infall time inference as long as the kernel is not an appreciable fraction of the domain (i.e. << 14 Gyr), at which point we are assuming the entire infall time distribution is drawn from a single gaussian, which is generally a poor assumption when selecting subhalos based on well constrained observational parameters for
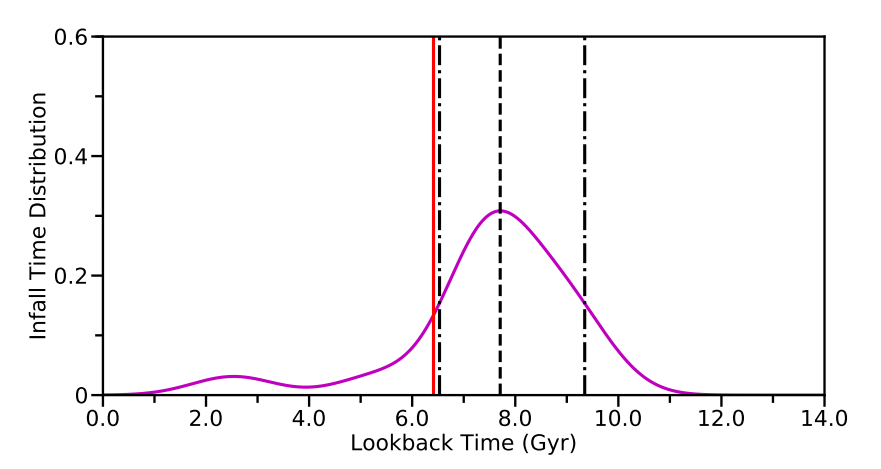
Figure 2. *Left*: The cumulative SFH for Leo II, adapted from Weisz et al. (2014), showing the adopted quenching time (solid red line) and adopted uncertainty on the quenching time (dashed red lines). *Right*: As an example of the infall time selection, we show the distribution of infall times for Leo II by selecting the 15 subhalos residing nearest to Leo II in the $\mathcal{E}$-distance space (see Fig. 1). The distribution of $t_{\rm infall}$) (magenta line) is smoothed with a gaussian kernel of width 0.8 to allow for a cleaner inference of the peak in the distribution. We adopt the peak in the distribution (black dashed line) as the characteristic infall time for Leo II. The accompanying dot-dashed lines illustrate the uncertainty in the inferred $t_{\rm infall}$ measure, corresponding to the width at 50% of the peak (FWHM). For reference, the red line shows the quenching time as derived from the star formation history in the *left* panel. **Briefly describe the quenching time - infall time situation for Leo II**.

specific MW dwarf galaxies. We adopt the peak in the smoothed distribution as the typical infall time for each Milky Way dwarf galaxy. To estimate the scatter in the infall times and host-to-host variation we adopt the width at 50% of the max (effectively the FWHM) as the uncertainty in the typical infall time.

2.3 Quenching Timescale

As discussed previously, we define the quenching timescale ($\tau_{\rm quench}$) as the time that a satellite continues to forms stars following infall. In other words, the quenching timescale is the difference between the infall time and the quenching time:

$$\tau_{\rm quench} = t_{\rm infall} - t_{\rm quench} \cdot \qquad (3)$$

When the quenching timescale is positive, this parameterization is ultimately an upper limit on the true quenching timescale as it includes what other work has called the "delay time" (Wetzel et al. 2013; McGee et al. 2014), or the time after infall where a satellite continues to form stars largely unabated. While the delay time appears to be significant at higher satellite stellar masses (Wetzel et al. 2013; McGee et al. 2014), at the low-mass scale of this work the quenching times are typically very short, such the delay times are effectively ~ 0 Gyr. In Table 1, we report the measured infall time and quenching time for each dwarf in our primary sample. The uncertainty in both the infall time and quenching time are added in quadrature in order to approximate the total uncertainty in the quenching timescale.

3 RESULTS

Figure 3 shows the quenching time as a function of infall time for every Milky Way satellite in our sample, color-coded by stellar mass. For the lowest mass systems ($M_\star \lesssim 10^5$ M$_\odot$), we find that the quenching time universally exceeds the infall time ($t_{\rm quench} > t_{\rm infall}$), such that the suppression of star formation preceded infall onto the Milky Way. In contrast, at higher satellite masses, quenching is found to occur at (or after) the time of infall ($t_{\rm quench} \lesssim t_{\rm infall}$). In

this manner, the quenching time–infall time space can be used to determine the class of quenching mechanisms potentially responsible for shutting down star formation. Specifically, objects that fall below and to the right of the dashed line in Figure **??** are consistent with environmental quenching, where star formation is quenched after the galaxy becomes a satellite. The distance from the dashed line in combination with how early (or late) infall time occurred, can further constrain which environmental quenching mechanisms are most likely responsible. The horizontal dot-dashed line at $t_{\rm quench} = 12.5$ Gyr ($z \sim 6$) marks the approximate location of the end of reionization. Galaxies with $t_{\rm quench}$ consistent with this value are potentially quenched during (or shortly after) the epoch of reionization. The remaining region in the $t_{\rm quench}$-$t_{\rm infall}$ space, above and to the left of the dashed line but below the dot-dashed line, favors quenching via feedback or some other internal process such that star formation is suppressed prior to infall.

Subtracting the quenching time from the infall time, we determine the quenching timescale ($\tau_{\rm quench}$) for every satellite galaxy in our primary sample (see Equation **??**). In Figure 4, we plot this quenching timescale, for each system, as a function of its stellar mass (cyan diamonds). For comparison, we include the results of several statistical studies that provide estimates of the typical quenching timescale for various satellite and host samples in the local Universe (see Fillingham et al. 2015; Wheeler et al. 2014; Wetzel et al. 2013, for a detailed description these works). Overall, the individual measures of $\tau_{\rm quench}$ for the MW satellites are in good agreement with these results. At $M_\star \gtrsim 10^{5.5}$ M$_\odot$, the positive quenching timescales are broadly consistent with the expectations from Fillingham et al. (2015). Meanwhile, the universally negative quenching timescales for the lowest mass systems ($M_\star \lesssim 10^{5.5}$ M$_\odot$) are consistent with quenching driven by reionization (Rodriguez Wimberly et al. 2018). *mcc – discuss the inclusion of LMC/SMC in Fig 4 here.*
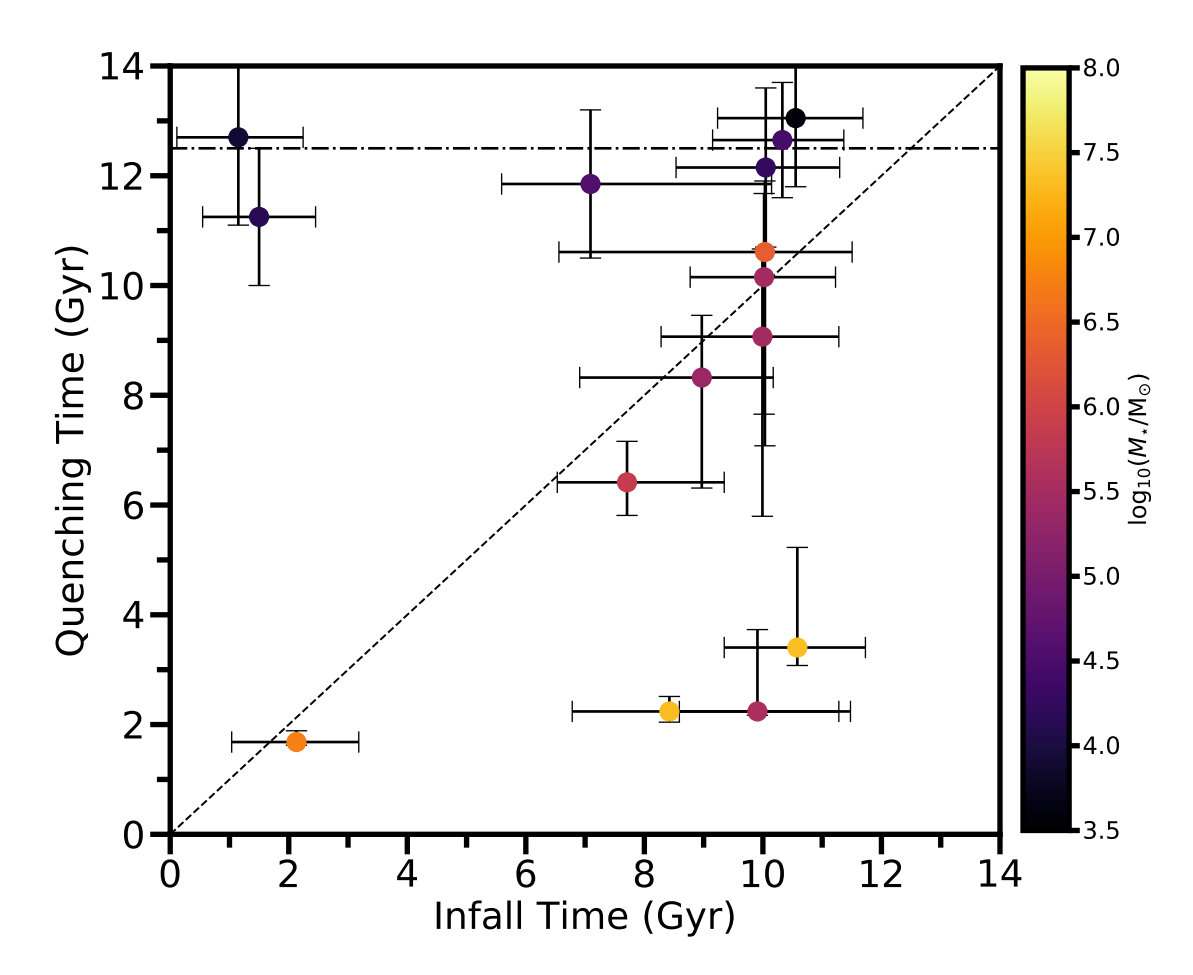
Figure 3. The quenching time, as determined from the SFHs, as a function of the lookback time to first infall for every dwarf galaxy in our sample. The points are color-coded by their present day stellar mass, assuming $M/L = 1$, see colorbar for scale. The errorbars are the width of the infall time distribution at 50% of the peak. Where objects are located in this space can help inform the potential quenching mechanisms responsible for shutting down star formation. The lower right region– relative to the dashed one-to-one line – is consistent with environmental quenching as the objects occupying this space fell onto the Milky Way before they quenched. The exact magnitude of the deviation from the dashed line can help inform the specific mechanisms responsible for their quenching, see § 4. The upper region, above the dot-dashed line, with quenching times older than ∼ 11 Gyr ago, is generally consistent with reionization quenching. These galaxies all had their star formation quenched at early times, while their infall times roughly span all of cosmic time. **Describe the potential for feedback quenching if objects occupy the remaining part of the parameter space. Finally, the remaining area, potentially containing CVn I, is consistent with *in situ* quenching. These objects quenched their star formation prior to infall, but the associated quenching times are relatively late for reionization to be expected to play a significant role, therefore requiring some other mechanism to shut down star formation, see § 4 for more details.**

4   DISCUSSION

4.1   Comparison to Previous Studies

- Include a comparison to Rocha et al. (2012) and Weisz et al. (2015)
    - What does VL2 look like in the BE-distance space?
    - My infall time vs Miguel's infall time object by object using 4D to show consistency and show how 6D improves the constraint.

4.2   Quenching at Low Masses

5   SUMMARY

In conclusion, this work highlights the power of combining detailed observations of galaxies in the nearby Universe with cosmological simulations....

    - Review the method in the context of Geha et al. (2012); Fillingham et al. (2015, 2018) results.

This work comes to the following conclusions:

- *Gaia* DR2 and the subequent data products allow for the remarkable ability to constrain infall time of the MW satellites, given our mapping of the binding energy to the infall time.
- Object-by-object measurements of quenching timescales agree with picture developed in (Fillingham et al. 2015, 2016, 2018), where environmental processes are responsible for satellite quenching for galaxies with $M_\star = 10^{6-8} \, M_\odot$.
- Galaxies with $M_\star \leq 10^5 \, M_\odot$ all have negative quenching timescales, indicating quenching prior to infall onto the MW, which is consistent with reionization being responsible for shutting down star formation.
- The data suggest that none of the MW satellites, with proper motion measurements and SFHs, are quenched via a secular process (e.g. feedback).
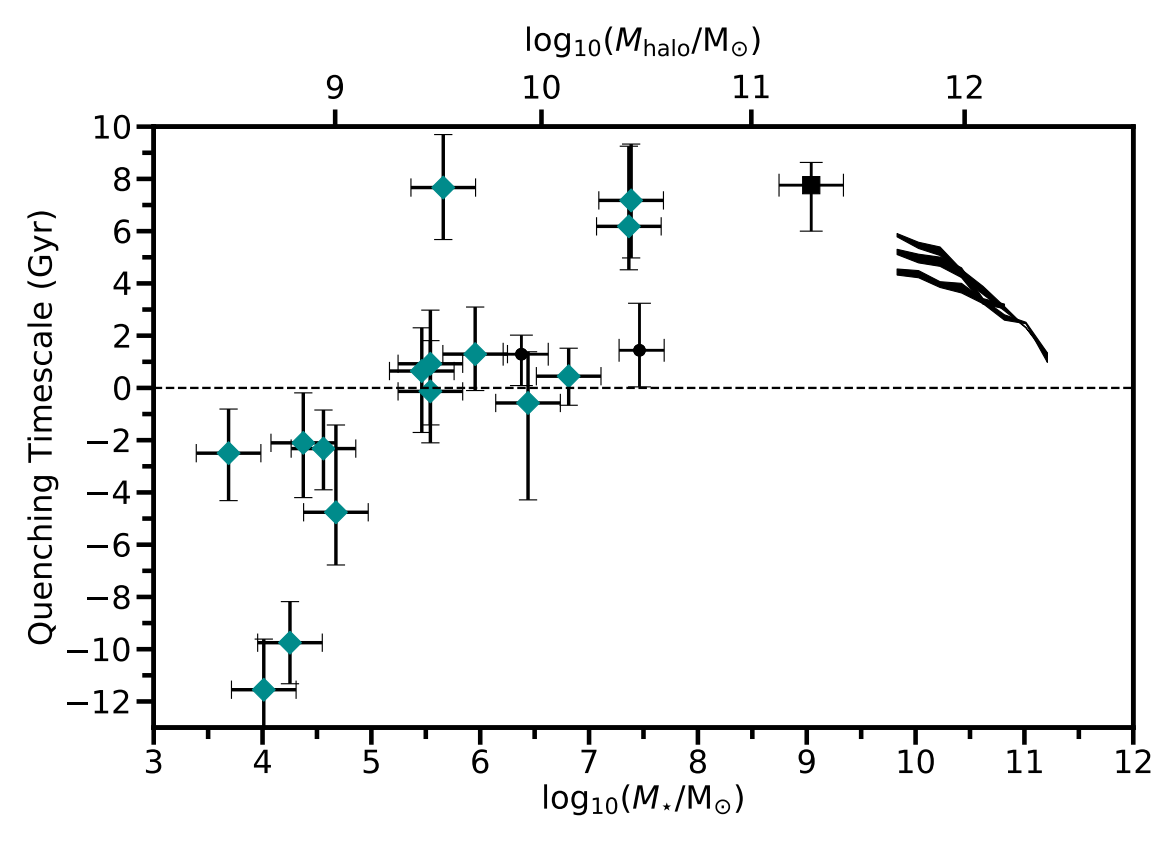
    - Any final caveats..?

Figure 4. *mcc – perhaps add a legend in the bottom right corner? and use faded, but varying, colors for the statistical points? also, include LMC/SMC limits* The quenching timescale as a function of satellite stellar mass for our primary sample of Milky Way dwarfs (cyan points). The black data points and bands illustrate the results of statistical studies of satellites in local groups and clusters (including the Local Group, Wetzel et al. 2013; Wheeler et al. 2014; Fillingham et al. 2015). Our measured quenching timescales, computed on an object-by-object basis, are broadly consistent with the results of statistical studies, such that satellites with $10^{5.5} \lesssim M_\star / M_\odot \lesssim 10^8$ have positive quenching timescales consistent with environmental quenching. Below this mass scale ($M_\star \lesssim 10^{5.5}$ M$_\odot$), our measured quenching timescales are systematically negative, consistent with a scenario in which the lowest-mass galaxies quench prior to infall (i.e. at the time of, or shortly following, reionization).

REFERENCES

Astropy Collaboration et al., 2013, A&A, 558, A33
Balogh M. L., et al., 2016, MNRAS, 456, 4364

Bland-Hawthorn J., Gerhard O., 2016, ARA&A, 54, 529
Brown T. M., et al., 2014, ApJ, 796, 91
Dark Energy Survey Collaboration et al., 2016, MNRAS, 460, 1270
Dolphin A., 1997, New Astron., 2, 397
Fillingham S. P., Cooper M. C., Wheeler C., Garrison-Kimmel S., Boylan-Kolchin M., Bullock J. S., 2015, MNRAS, 454, 2039
Fillingham S. P., Cooper M. C., Pace A. B., Boylan-Kolchin M., Bullock J. S., Garrison-Kimmel S., Wheeler C., 2016, MNRAS, 463, 1916
Fillingham S. P., Cooper M. C., Boylan-Kolchin M., Bullock J. S., Garrison-Kimmel S., Wheeler C., 2018, MNRAS, 477, 4491
Fritz T. K., Battaglia G., Pawlowski M. S., Kallivayalil N., van der Marel R., Sohn T. S., Brook C., Besla G., 2018, preprint, (arXiv:1805.00908)
Gaia Collaboration et al., 2016a, A&A, 595, A1
Gaia Collaboration et al., 2016b, A&A, 595, A2
Gaia Collaboration et al., 2018b, preprint, (arXiv:1804.09381)
Gaia Collaboration Brown A. G. A., Vallenari A., Prusti T., de Bruijne J. H. J., Babusiaux C., Bailer-Jones C. A. L., 2018a, preprint, (arXiv:1804.09365)
Geha M., Blanton M. R., Yan R., Tinker J. L., 2012, ApJ, 757, 85
Grcevich J., Putman M. E., 2009, ApJ, 696, 385
Haines C. P., Gargiulo A., Merluzzi P., 2008, MNRAS, 385, 1201
Hunter J. D., 2007, Computing In Science & Engineering, 9, 90
Irwin M. J., 1994, in Meylan G., Prugniel P., eds, European Southern Observatory Conference and Workshop Proceedings Vol. 49, European Southern Observatory Conference and Workshop Proceedings. p. 27
Jones E., Oliphant T., Peterson P., et al., 2001, SciPy: Open source scientific tools for Python, http://www.scipy.org/

Kallivayalil N., et al., 2018, preprint, (arXiv:1805.01448)

Lin D. N. C., Faber S. M., 1983, ApJ, 266, L21

Massari D., Helmi A., 2018, preprint, (arXiv:1805.01839)

Mateo M. L., 1998, ARA&A, 36, 435

McConnachie A. W., 2012, AJ, 144, 4

McGee S. L., Bower R. G., Balogh M. L., 2014, MNRAS, 442, L105

Navarro J. F., Frenk C. S., White S. D. M., 1997, ApJ, 490, 493

Pace A. B., Li T. S., 2018, preprint, (arXiv:1806.02345)

Pedregosa F., et al., 2011, Journal of Machine Learning Research, 12, 2825

Pérez F., Granger B. E., 2007, Computing in Science and Engineering, 9, 21

Phillips J. I., Wheeler C., Cooper M. C., Boylan-Kolchin M., Bullock J. S., Tollerud E., 2015, MNRAS, 447, 698

Planck Collaboration et al., 2016, A&A, 594, A13

Rocha M., Peter A. H. G., Bullock J., 2012, MNRAS, 425, 231

Rodriguez Wimberly M. K., Cooper M. C., Fillingham S. P., Boylan-Kolchin M., Bullock J. S., Garrison-Kimmel S., 2018, preprint, (arXiv:1806.07891)

Simon J. D., 2018, preprint, (arXiv:1804.10230)

Slater C. T., Bell E. F., 2014, ApJ, 792, 141

Spekkens K., Urbancic N., Mason B. S., Willman B., Aguirre J. E., 2014, ApJ, 795, L5

Tollerud E. J., Bullock J. S., Strigari L. E., Willman B., 2008, ApJ, 688, 277

Walt S. v. d., Colbert S. C., Varoquaux G., 2011, Computing in Science & Engineering, 13

Weisz D. R., et al., 2011, ApJ, 739, 5

Weisz D. R., Dolphin A. E., Skillman E. D., Holtzman J., Gilbert K. M., Dalcanton J. J., Williams B. F., 2014, ApJ, 789, 147

Weisz D. R., Dolphin A. E., Skillman E. D., Holtzman J., Gilbert K. M., Dalcanton J. J., Williams B. F., 2015, ApJ, 804, 136

Weisz D. R., Dolphin A. E., Skillman E. D., Holtzman J., Gilbert K. M., Dalcanton J. J., Williams B. F., 2017, VizieR Online Data Catalog, 178

Wetzel A. R., Tinker J. L., Conroy C., van den Bosch F. C., 2013, MNRAS, 432, 336

Wetzel A. R., Tollerud E. J., Weisz D. R., 2015, ApJ, 808, L27

Wheeler C., Phillips J. I., Cooper M. C., Boylan-Kolchin M., Bullock J. S., 2014, MNRAS, 442, 1396

York D. G., et al., 2000, AJ, 120, 1579